The 2022 super-Eddington outburst of the source SMC X-2

M. J. Coe,[1]★ J. A. Kennea[2], I. M. Monageng[3,4], L.J. Townsend[3,5], D.A.H. Buckley[3,4],
M. Williams[2], A. Udalski[6] and P. A. Evans[7]

[1]*Physics & Astronomy, The University of Southampton, Southampton, SO17 1BJ, UK*
[2]*Department of Astronomy and Astrophysics, The Pennsylvania State University, 525 Davey Lab, University Park, PA 16802, USA*
[3]*South African Astronomical Observatory, P.O Box 9, Observatory, 7935, Cape Town, South Africa*
[4]*Department of Astronomy, University of Cape Town, Private Bag X3, Rondebosch 7701, South Africa*
[5]*Southern African Large Telescope, Cape Town, South Africa*
[6]*Astronomical Observatory, University of Warsaw, Al. Ujazdowskie 4, 00-478 Warszawa, Poland*
[7]*University of Leicester, X-ray and Observational Astronomy Research Group, School of Physics & Astronomy, University Road, Leicester LE1 7RH, UK.*

ABSTRACT

SMC X-2 exhibits X-ray outburst behaviour that makes it one of the most luminous X-ray sources in the Small Magellanic Cloud. In the last decade it has undergone two such massive outbursts - in 2015 and 2022. The first outburst is well reported in the literature, but the 2022 event has yet to be fully described and discussed. That is the goal of this paper. In particular, the post-peak characteristics of the two events are compared. This reveals clear similarities in decay profiles, believed to be related to different accretion mechanisms occurring at different times as the outbursts evolve. The Hα emission line indicates that the Be disc undergoes complex structural variability, with evidence of warping as a result of its interaction with the neutron star. The detailed observations reported here will be important for modelling such interactions in this kind of binary systems.

Key words: stars: emission line, Be X-rays: binaries

1 INTRODUCTION

SMC X-2 is a high-mass X-ray binary system located in the Small Magellanic Cloud (SMC), a satellite galaxy of the Milky Way. The system consists of a neutron star and a massive companion star, which are orbiting each other in a close binary system.

The neutron star in SMC X-2 is a highly compact object with a mass approximately 1.4 times that of the sun, but a radius of only a few kilometers. The companion star is a massive OB-type star, which is a type of hot, luminous star that emits strong Balmer lines in its spectrum due to the presence of a circumstellar disk of gas.

The binary system is slightly eccentric (e=0.07), with an orbital period of 18.4 days (Townsend et al. 2011). As the two stars orbit each other, material from the companion star's circumstellar disc is pulled towards the neutron star due to its strong gravitational field. This material may form a transient accretion disk around the neutron star, which emits X-rays as it is heated up and undergoes gravitational interactions with the neutron star.

SMC X-2 is an important object of study for astrophysicists because it is a high-mass X-ray binary system (HMXB), which is a class of objects that are thought to be provide significant sources of X-rays in the universe. The system is also notable for exhibiting a range of complex X-ray variability. These include regular 2.37s pulsations from the neutron star, as well as more erratic variability that is likely

caused by changes in the circumstellar disc size and hence accretion rate onto the neutron star.

The first reported super-Eddington outburst for SMC X-2 was in 2000 (Corbet et al. 2001). It then underwent an extended period of quiescence until 15 years later when the system exhibited another major X-ray outburst reaching X-ray luminosities well in excess of 10^{38} erg/s. Observational reports and follow-up discussions of this particular outburst may be found in the following papers: Lutovinov et al. (2017), Li et al. (2016), Fotopoulou et al. (2015), La Palombara et al. (2016), Kennea et al. (2015), Roy et al. (2022) and Jaisawal et al. (2023). 7 years later the source underwent the next major X-ray outburst which is reported in this paper. Though this 2022 outburst didn't quite reach the same X-ray peak luminosity as the 2015 event it nonetheless again exceeded 10^{38} erg/s and hence represents a substantial occurrence. In this work we report a multiwaveband study of this event and make important comparisons with the earlier 2015 X-ray outburst.

2 OBSERVATIONS

2.1 Swift X-ray Observations

The S-CUBED project (Kennea et al. 2018) started regular observations using the Swift X-ray Telescope (XRT; Burrows et al. 2005) of the Small Magellanic Cloud in July 2016 in order to watch for X-ray outbursts from BeXRB systems. As part of this project SMC X-2 has been observed approximately weekly in the 0.3-10 keV band,

★ E-mail: mjcoe@soton.ac.uk
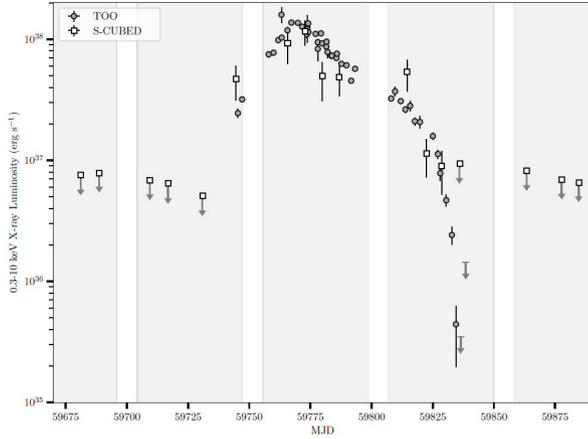
Figure 1. Combined S-CUBED and TOO X-ray light-curve of SMC X-2, showing the 2022 outburst period. Grey background regions show periods of time when the source was observable by Swift, white gaps are observing gaps due to spacecraft constraints. The similarity of the 2022 outburst profile can be compared to the 2015 outburst profile (see Fig. 1 from Lutovinov et al. (2017)).

although the majority of these observations are only 60s exposure. We note that the previous outburst of SMC X-2 was in 2015, and was tracked extensively by Swift through Target of Opportunity (TOO) observations, however this outburst was over before the S-CUBED project began.

On June 14th, 2022 data from S-CUBED showed a point source at the location of SMC X-2 detected in 38s of Photon Counting (PC) mode XRT data, significantly above all previous upper limits found in S-CUBED monitoring of this source Kennea et al. (2022). This indicated that SMC X-2 was likely entering a new outburst phase.

Due to the detection of this new outburst observations were requested through the Swift Target of Opportunity (TOO) program, consisting of initially daily, followed by every 2 day observations with a requested exposure time of 1ks per exposure. Observations were taken in a combination of PC and Windowed Timing (WT) modes for XRT, based on predicted X-ray brightness. These TOO observations continued until SMC X-2 was no longer detectable by Swift, with the final observation taken on September 19th, 2022. Alongside these TOO observations, S-CUBED regular monitoring of the source continued.

A table of TOO observations is given in Table A1 and the resulting measurements displayed in Fig. 1.

Fig. 2 shows the X-ray decay profiles of the 2022 outburst overlaid on the profile for the 2015 one. To produce this merged plot the 2015 data timings have been arbitrarily adjusted by -57280d and the 2022 data by -59740d. There has been no attempt to precisely match the data sets, but rather a small offset has been chosen so that both data sets can be clearly seen to follow similar decay patterns. Though the peak fluxes differ by a factor of two, the decay profiles are extremely similar. In both cases there is a distinct change in the decay slope around the 60d mark in the figure. These decay profiles are discussed further below.

2.2 UV and optical photometry

The UltraViolet and Optical Telescope (UVOT) uvw1 filter (2600Å) data were analyzed using the Swift ftools available in HEASOFT version 6.30. Images with multiple snapshots were summed with
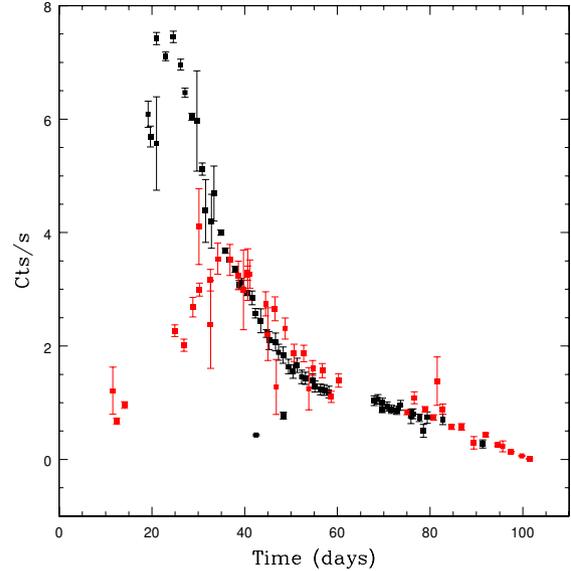
Figure 2. The X-ray profiles (XRT counts/s in 0.3-10 keV range) of the 2015 outburst (black) overlaid on top of the 2022 outburst discussed in this paper (red). The 2022 data is the same as that presented in Fig. 1, but on a linear scale and in flux units.

uvotimsum. Photometry was then performed using uvotsource with a source region of radius 5” and a larger source-free background region. Images that were not aligned with the World Coordinate System were first aspect corrected using uvotunicorr before being analyzed as previously described. The resulting lightcurve is shown in Fig. 3

The OGLE project (Udalski et al. 2015) provides long term I-band photometry with a cadence of 1-3 days. I band data were collected on the optical counterpart to SMC X-2 as part of the OGLE IV project from JD 2455346 till JD 2458759. The OGLE identification for this object is SMC720.17.50. These results are also shown in Fig. 3.

2.3 Optical spectroscopy

The optical counterpart to SMC X-2 was observed with the Southern African Large Telescope (SALT; Buckley et al. 2006) using the Robert Stobie Spectrograph (RSS; Burgh et al. 2003; Kobulnicky et al. 2003) and the High-Resolution Spectrograph (HRS; Bramall et al. 2010, 2012; Crause et al. 2014). The RSS observations were performed using various grating settings: PG0900, PG1800 and PG2300. A summary of the settings is provided in Table 1. The primary reductions (which comprise overscan correction, bias subtraction, gain correction and amplifier cross-talk corrections) were performed using the SALT pipeline (Crawford et al. 2012). The remaining data reduction steps (arc line identification, background subtraction and 1D spectrum extraction) were executed using IRAF[1]. The HRS observations were carried out in low-resolution mode ($R \sim 14000$), where exposure times of 1200 s were used. A wavelength coverage of 3750–8790 Å was obtained. The SALT pipeline was used for the primary reductions, while the remaining reduction steps ((background subtraction, identification of arc lines, blaze function removal, and merging of the orders) were done using the MIDAS

---

[1] Image Reduction and Analysis Facility: iraf.noao.edu
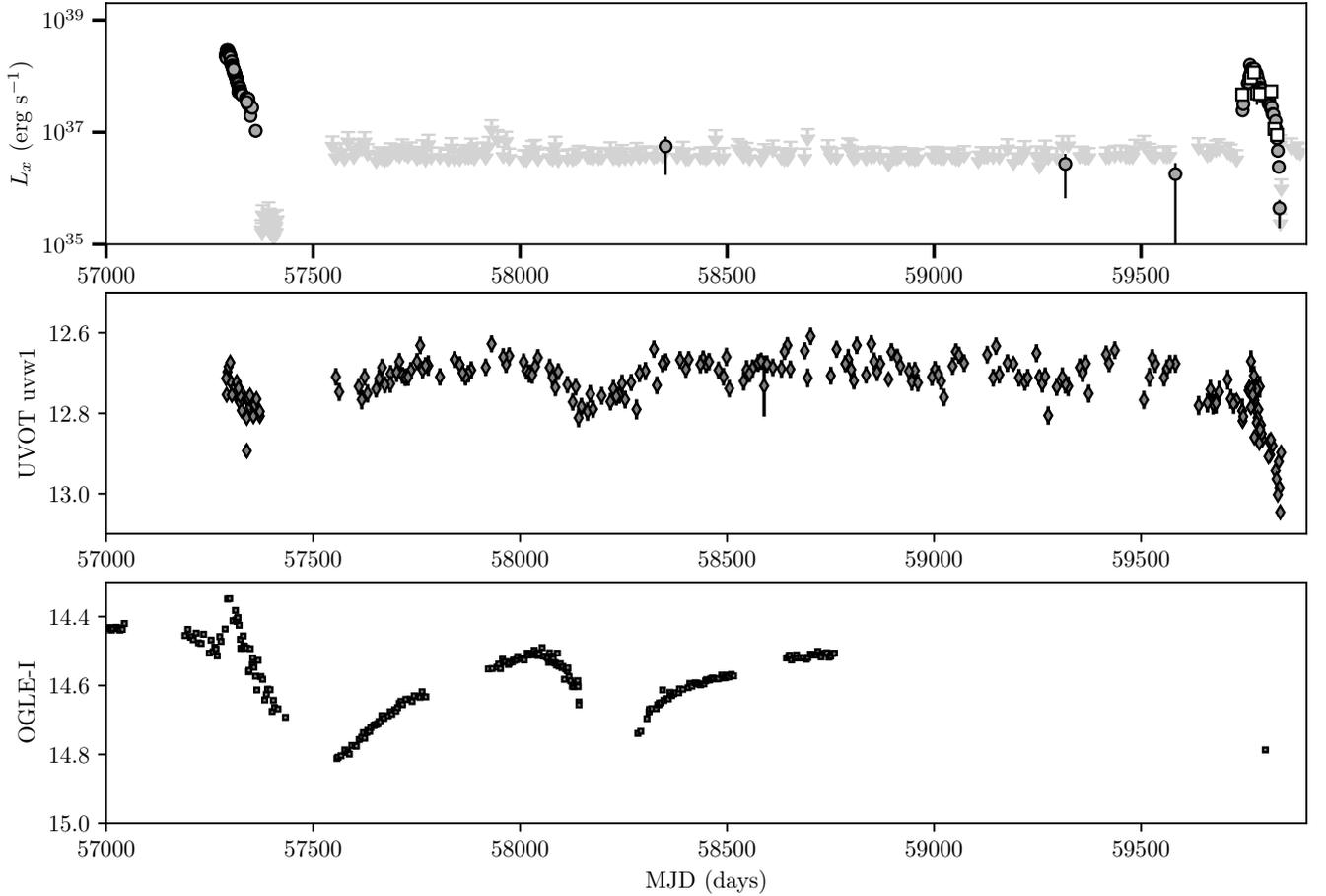
Figure 3. 8 year time history of Swift XRT 0.3-10 keV (top panel), UVOT uvw1 filter (middle panel), with OGLE I-band lightcurve plotted for comparison (bottom panel). The 2015 outburst covers the period MJD 57300 - 57450, and the 2022 outburst MJD 59750 - 58400.

Table 1. A summary of the settings for the SALT RSS observations

Grating	Grating angle	Wavelength range (Å)	Exposure time (s)
PG0900	12.5/14.75	4070 − 7000	120/600
PG1800	36.5	5900 − 7200	240
PG2300	48.875	6100 − 6900	1800

FEROS (Stahl et al. 1999) and ECHELLE (Ballester 1992) packages. The full details of the data reduction process are described in Kniazev et al. (2016).

A log of the observations and the inferred Hα equivalent width (EW) measurements are shown in Table A2. An example of the Hα emission line profile is shown in Fig. 4.

However, obtaining a reliable assessment of the true strength of the Hα EW for SMC X-2 is difficult. The optical counterpart has been shown to have a very close, similar star on the sky, separated by just ~1 arcsecond (Murdin et al. 1979). Those authors report that the nearby star is an O7 type object, which means it probably has an Hα EW of +(3.0–3.4)Å (Conti 1974). The vast majority of the

SALT spectra were obtained whilst the seeing conditions were 1-2 arcsec, therefore it is probable that there is some contamination of the determined Hα EW values for SMC X-2 by up to this amount. If the O7 star does not have a circumstellar disc, and hence does not exhibit variable Hα EW, then the estimates presented here of the Hα EW for SMC X-2 could be misrepresented in magnitude by up to +3Å. So it cannot be assumed that any apparent changes in this parameter from SMC X-2 are real if the changes are less than ~3Å.

2.4 MeerKAT

We obtained three observations of SMC X-2 with MeerKAT during its outburst. The observations were performed at a central frequency of 1.28 GHz, bandwidth of 856 MHz and an integration time of 8 s. Each observation consisted of a total of 60-minute scans on target. J0408-6545 was used as a primary calibrator, where it was observed at the start and end of each scan. The secondary calibrator, J0252-7104, was observed in 2-minute scans for every 20-minute on the target. The data were processed using the OxKAT reduction routines (Heywood
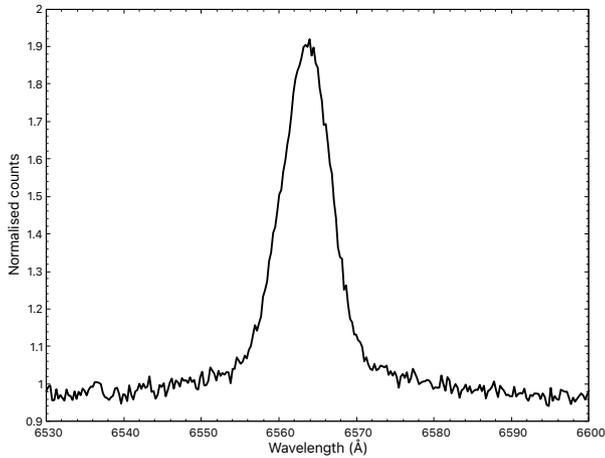
Figure 4. An example of the Hα emission line in SMC X-2 from an RSS observation obtained on 07-08-2022 (MJD59798.07).

Date	MJD	Radio flux density (μJy)
2022-06-19	59749.5	< 38.4
2022-07-10	59770.5	< 38.6
2022-07-18	59778.5	< 34.9

Table 2. MeerKAT (1.28 GHz) 3σ upper limits.

2020)[2], which performs averaging, application of standard bandpass and gain corrections, and flagging. The imaging was executed using WSCLEAN, after which a self-calibration cycle was performed. All three observations resulted in non-detections at the optical position of SMC X-2 . A log of the 3σ upper limits is given in Table 2. The radio emission during peak outburst is believed to be due to the launch of an accretion-powered jet in these systems (e.g. van den Eijnden et al. 2021, 2022). However, the current sensitivity of instruments is inadequate to detect jet emission at extragalactic distances. The increased sensitivity from future radio telescopes in the Southern hemisphere is expected to probe the jet-launching mechanism.

3 DISCUSSION

3.1 X-ray decay profiles

Fig. 2 shows the combined X-ray decay profiles of the 2015 and 2022 outbursts. Simple linear best fits have been applied to the two phases of the decay with a break at 40d (TJD 57320 for the 2015 outburst and TJD 52513 for the 2022 event). This break corresponds to a XRT count rate of ~1.5 cts/s, or a luminosity in the SMC of $\sim 5 \times 10^{37}$ erg/s. At this point the the decay profile slope completely changes and flattens by a factor of ~6.5. Other simple models were explored to fit the decay section of the S-CUBED data such as an exponential fit. Such a fit works well for the first section of the data, but after the 40d point the data indicate a flatter decay profile. Clearly more sophisticated modelling beyond the scope of this paper are required.

There is also a suggestion of an even steeper decay rate during the first 10-15d of the 2015 outburst, that switch occurring at a luminosity of $\sim 1.5 \times 10^{38}$ erg/s. Unfortunately the 2022 outburst did not reach

2 https://github.com/IanHeywood/oxkat

such high luminosities so we cannot comment on such a steep profile component.

These changes in decay profile rates almost certainly indicate significant changes in the mode of accretion on to the neutron star. Lutovinov et al. (2017) studied the changing decay profile of the 2015 outburst and concluded that there was a change of accretion mode to the propeller mode (Illarionov & Sunyaev 1975) at a luminosity of 4×10^{36} erg/s which corresponds to an XRT count rate of ~0.1 cts/s on Fig. 2. This is at the very end of the outburst, at which point they show that the X-ray flux dropped significantly. There is no doubt that this is the end of the outburst but it is at the limit of the sensitivity of the Swift XRT telescope. Important to their model are the upper limits set immediately after the final positive detection since they help define the shape of the final decay phase. They set the upper limit for any detection as low as 2×10^{34} erg/s. Unfortunately the data presented here are less sensitive and are only able to set a limit an order of magnitude higher - see Fig. 1.

Tsygankov et al. (2016) investigated the switching on/off of the propeller effect in two other BeXRBs- 4U 0115+63 and V 0332+53. In both cases they interpreted the tail end of the outburst decays to indicate an accretion transition around $(1 - 2) \times 10^{36}$ erg/s. It is interesting to see the visual difference that presenting the data on a logarithmic scale (e.g. Fig. 1) as compared to a linear scale (e.g. Fig. 2). Plus the difficulties of fitting models that rely on the limiting sensitivity of the telescope - see, for example, the results presented by Tsygankov et al. (2016) on the source V 0332+53 (their Figure 2). The manner of the data presented here focuses strongly on the times of very significant source detection, and the resulting change in decay rates seen at $\sim 5 \times 10^{37}$ erg/s. This is unlikely to be a switch to the propeller regime since the flux does not drop dramatically, but it certainly indicates that something significant has happened that deserves further modelling investigations beyond the scope of this paper. Finally, it is worth noting that the binary period for this system is 18.4d with a slight eccentricity of 0.07 (Townsend et al. 2011), so throughout the observational period being discussed here (~70d) the distance between the neutron star and the fuel source, the circumstellar disc, is constantly varying. So, inevitably, the accretion environment being experienced by the neutron star is also constantly changing. This factor also needs to be included in any models.

3.2 Optical photometric variability

3.2.1 Long-term UVOT uvw1 and I band lightcurves

The evolution of the UVOT uvw1 and OGLE I-band brightness taken over a period of ~8 years is shown in the bottom 2 panels of Fig. 3. The lightcurves reveal long-term variability that is an indicator of structural changes happening in the inner and outer regions of the disc.

Both the uvw1 and I-band magnitudes generally show correlated changes with respect to the X-ray lightcurve. This is particularly evident during the decline of both the 2015 and 2022 X-ray outbursts. The I-band lightcurve shows a sharp spike at the onset of the 2015 X-ray outburst, which suggests that the neutron star distorted the outer parts of the disc which resulted in the matter being accreted, leading to enhanced X-ray activity. This behaviour was discussed by Roy et al. (2022). Similarly, an enhanced spike in the uvw1 lightcuve is observed at the start of the 2022 X-ray outburst followed by a drop in flux as the X-ray outburst decays. During the decay of the 2015 X-ray outburst, the I-band brightness is seen to decrease at a faster rate than the uvw1. This is unsurprising since the I-band magnitude is a tracer of the more extended, outer regions of the disc

compared to the uvw1 magnitude which measures the changes in the inner disc regions. It is often noted that the longer wavelength filters (i.e. the I-band) undergo larger amplitude changes compared to those at the shorter wavelengths in BeXBs (e.g. Reig & Fabregat 2015; Coe et al. 2022). This behaviour indicates global disruption of the disc from the outer to inner parts as a result of the interaction of the disc with the neutron star. A noticeable feature of Fig. 3 during the simultaneous uvw1 and I-band observations is the time lag in reaching peak brightness in the two bands between MJD57900 and MJD58100. The innermost region of the disc reaches peak brightness ~150 days before the outermost parts of the disc, indicative of the time taken for the effects of a mass ejection to reach the outer limits of the disc.

3.2.2 (uvw1-I) colour variability

The top panel of Fig. 5 shows the evolution of the (uvw1-I) colour for the period where there are simultaneous uvw1- and I-band observations. The colour is a proxy for the disc temperature, with the blue and red colours indicating hotter and cooler temperatures, respectively. During the period between MJD57300 and MJD57400 the overall (uvw1-I) colour evolves to lower (bluer) values, indicating an overall temperature increase. This is the period when the overall brightness was undergoing a decline (Fig. 3) during the decay of the 2015 X-ray outburst. This suggests that the outer, cooler parts of the disc were lost due to the neutron star interaction. The overall trend of the (uvw1-I) colour between MJD57600 and MJD58800 is increasing (the colour is reddening) since this is the period when the disc is increasing in size and there is therefore a larger contribution of cooler temperatures as the outer regions extend outwards.

As circumstellar discs in BeXBs grow in size they generally show an excess flux and their red continuum increases. The reddening of the system with disc growth is attributed to the outer parts of the disc being cooler than the inner parts (Harmanec 1983). When viewed at low/intermediate angles, a correlation between the brightness and colour (i.e. temperature) would be observed. Discs that are viewed at an edge-on orientation (high inclination angles) would exhibit an anti-correlation between the brightness and colour. In this geometry, as the disc grows in size the overall brightness of the Be disc/star system decreases since the flaring disc blocks out some of the light from the Be star (Harmanec 1983; Rajoelimanana et al. 2011; Reig & Fabregat 2015). Fig. 5 (bottom panel) shows the $(uvw1 - I) - I$ colour-magnitude plot for the optical counterpart of SMC X-2. A strong correlation is observed between the $(uvw1 - I)$ colour and the brightness, which indicates an intermediate/low inclination angle of the disc. This is corroborated by the morphology of the Hα emission line in Fig. 4, which does not show a shell profile with a central depression that goes below the continuum, as is conventionally seen in highly-inclined disc orientations (Reig & Fabregat 2015).

3.3 Optical spectroscopic variability

Using Kepler's laws we estimate the semi-major axis and periastron passage of the neutron star, assuming the canonical neutron star mass ($M_X \sim 1.4$ M$_\odot$) and a Be star mass of $M_\star \sim 24$ M$_\odot$ based on its spectral type (Straizys & Kuriliene 1981). The orbital parameters ($P = 18.38$ d and $ecc = 0.07$) derived by Townsend et al. (2011) were used for the calculations. Using these parameters we find values of 86.20 ± 0.10 R$_\odot$ and 80 ± 2 R$_\odot$ for the semi-major axis and periastron passage, respectively.
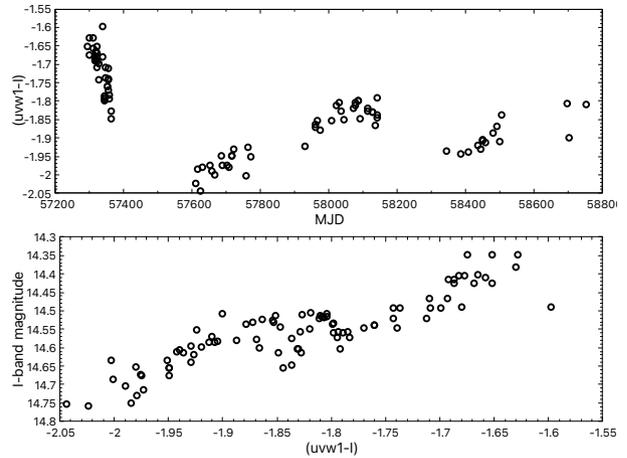
Figure 5. Top panel: The evolution of the $(uvw1 - I) - I$ colour. Bottom panel: $(uvw1 - I) - I$ colour–magnitude diagram.

Using the method of Hanuschik (1989), we estimate the size of the disc from the largest measured equivalent width (13.15 Å), which hopefully has the least contamination from the nearby O7 star. It gives a maximum radius that is larger than the periastron distance of the neutron star orbit (111 ± 7 R$_\odot$).

In Fig. 6 we show the evolution of residual Hα emission line spectra. To obtain these, we first created a model emission line by fitting a Voigt function to each spectrum and then subtracted the observed spectra from the model. Since the Voigt model approximates emission from an axisymmetric circumstellar disc, the resultant residual is a measure of deviation from axisymmetry. For the analysis we only consider observations taken with the PG2300 grating, as the resolution from the PG0900 and PG1800 is insufficient to study the morphological behaviour of the disc. Evidence of deviation from symmetry is seen before the 2022 X-ray outburst, at MJD58002.95, as there is a residual structure that shows up as a peak on the redshifted side of the line. This residual profile is seen to develop into a double-peak profile in the subsequent observations until MJD58395.93. The redshifted peak is seen to develop again during the peak of the 2022 X-ray outburst (MJD59773.12). The subtle variability in the residual profile continued as the outburst declined until MJD59831.93 when a pronounced double-peaked structure is seen that persists until the end of the outburst. This is a possible indicator of a complex non-uniform structure at the outer parts of the disc.

The semi-major axis can be calculated using the orbital parameters above, which when combined with the projected semi-major axis, $a_X \sin i_{\rm orbit} \sim 32$ R$_\odot$ (Townsend et al. 2011), can be used to estimate the inclination angle ($i_{\rm orbit} \sim 22°$) of the plane of the neutron star orbit. The disc radius can be estimated using the double-peaked Hα emission from the relation (Huang 1972):

$$R_{CS} = \frac{GM_\star \sin^2 i_{\rm disc}}{(0.5\Delta V)^2},$$ (1)

where:

- G - gravitational constant
- $M_\star$ - mass of the Be star
- $i_{\rm disc}$ - inclination angle of the disc
- ΔV - peak separation

The peak separation, ΔV, is measured by fitting a two-peak Voigt profile to the double-peaked emission lines and using the central

wavelengths of the fitted peaks in the calculation. Assuming that the residual component of the disc extends out to the outer edges, up to a radius of around 100 $R_\odot$, using Equation 1 and the spread of measured peak separations ($\sim 250 - 300$ km/s) gives a range of $35 - 45°$ for the outer edge inclination angles. This misalignment between the plane of the orbit of the neutron star and the plane of the Be disc can result in the warping of the outer disc edges. This is especially true when the circumstellar disc has grown to a size approaching that of the neutron star orbit.

4 CONCLUSIONS

The source SMC X-2 has shown three major outbursts in the last two decades - in 2000, 2015 and 2022. The one reported here which occurred in 2022 though not quite as X-ray bright as the 2015 event, is, however, well-documented at multiple wavelengths. At its peak it exceeded the traditional Eddington Limit with an X-ray luminosity of over 10^{38} erg/s, and triggered supporting optical & UV observations, both spectroscopic and photometric. It is only by integrating all these different multi-wavelength data sets together that valuable insights are obtained into both the details of the accretion physics of neutron stars, as well as the dynamic behaviour pattern of the companion Be star that triggered the whole event. The evidence that the Be star triggered the 2022 X-ray outburst is the contemporaneous sharp rise in the UV flux reported here - indicative of a major mass ejection from the star. This is the fuel for accretion onto the neutron star and the resulting X-ray outburst. Such behaviour is well established in other BeXRB systems - see, for example, Kennea et al. (2020) and Monageng et al. (2019).

The characteristics of the 2015 and 2022 decay profiles are compared revealing clear similarities, including a significant change in the rate of decay believed to be related to differing accretion mechanisms occurring at different times. The Hα emission line profiles indicates that the Be disc undergoes complex structural variability during the outburst, with evidence of warping as a result of its interaction with the neutron star. The detailed observations reported here will be important for more sophisticated modelling of such interactions in BeXRB systems, perhaps using Smooth Particle Hydrodynamics (see, for example, Brown et al. (2019)).

DATA AVAILABILITY

All X-ray data are freely available from the NASA Swift archives. The OGLE optical data in this article will be shared on any reasonable request to Andrzej Udalski of the OGLE project.

REFERENCES

Ballester P., 1992, in Grosbøl P. J., de Ruijsscher R. C. E., eds, European Southern Observatory Conference and Workshop Proceedings Vol. 41,

European Southern Observatory Conference and Workshop Proceedings. p. 177
Bramall D. G., et al., 2010, in Ground-based and Airborne Instrumentation for Astronomy III. p. 77354F, doi:10.1117/12.856382
Bramall D. G., et al., 2012, in McLean I. S., Ramsay S. K., Takami H., eds, Society of Photo-Optical Instrumentation Engineers (SPIE) Conference Series Vol. 8446, Ground-based and Airborne Instrumentation for Astronomy IV. p. 84460A, doi:10.1117/12.925935
Brown R. O., Coe M. J., Ho W. C. G., Okazaki A. T., 2019, MNRAS, 488, 387
Buckley D. A. H., Swart G. P., Meiring J. G., 2006, in Society of Photo-Optical Instrumentation Engineers (SPIE) Conference Series. p. 62670Z, doi:10.1117/12.673750
Burgh E. B., Nordsieck K. H., Kobulnicky H. A., Williams T. B., O'Donoghue D., Smith M. P., Percival J. W., 2003, in Iye M., Moorwood A. F. M., eds, Society of Photo-Optical Instrumentation Engineers (SPIE) Conference Series Vol. 4841, Proc. SPIE. pp 1463–1471, doi:10.1117/12.460312
Burrows D. N., et al., 2005, Space Sci. Rev., 120, 165
Coe M. J., et al., 2022, MNRAS, 513, 5567
Conti P. S., 1974, ApJ, 187, 539
Corbet R. H. D., Marshall F. E., Coe M. J., Laycock S., Handler G., 2001, ApJ, 548, L41
Crause L. A., et al., 2014, in Ground-based and Airborne Instrumentation for Astronomy V. p. 91476T, doi:10.1117/12.2055635
Crawford S. M., et al., 2012, PySALT: SALT science pipeline, Astrophysics Source Code Library (ascl:1207.010)
Fotopoulou S., Coe M. J., Bird A. J., McBride V., Bozzo E., 2015, The Astronomer's Telegram, 8207, 1
Hanuschik R. W., 1989, Ap&SS, 161, 61
Harmanec P., 1983, Hvar Observatory Bulletin, 7, 55
Heywood I., 2020, oxkat: Semi-automated imaging of MeerKAT observations (ascl:2009.003)
Huang S.-S., 1972, ApJ, 171, 549
Illarionov A. F., Sunyaev R. A., 1975, A&A, 39, 185
Jaisawal G. K., et al., 2023, MNRAS, 521, 3951
Kennea J. A., et al., 2015, The Astronomer's Telegram, 8091, 1
Kennea J. A., Coe M. J., Evans P. A., Waters J., Jasko R. E., 2018, ApJ, 868, 47
Kennea J. A., Coe M. J., Evans P. A., Monageng I. M., Townsend L. J., Siegel M. H., Udalski A., Buckley D. A. H., 2020, MNRAS, 499, L41
Kennea J. A., Coe M. J., Evans P. A., 2022, The Astronomer's Telegram, 15434, 1
Kniazev A. Y., Gvaramadze V. V., Berdnikov L. N., 2016, MNRAS, 459, 3068
Kobulnicky H. A., Nordsieck K. H., Burgh E. B., Smith M. P., Percival J. W., Williams T. B., O'Donoghue D., 2003, in Iye M., Moorwood A. F. M., eds, Proc. SPIE Vol. 4841, Instrument Design and Performance for Optical/Infrared Ground-based Telescopes. pp 1634–1644, doi:10.1117/12.460315
La Palombara N., Sidoli L., Pintore F., Esposito P., Mereghetti S., Tiengo A., 2016, MNRAS, 458, L74
Li K. L., Hu C. P., Lin L. C. C., Kong A. K. H., 2016, ApJ, 828, 74
Lutovinov A. A., Tsygankov S. S., Krivonos R. A., Molkov S. V., Poutanen J., 2017, ApJ, 834, 209
Monageng I. M., et al., 2019, MNRAS, 489, 993
Murdin P., Morton D. C., Thomas R. M., 1979, MNRAS, 186, 43P
Rajoelimanana A. F., Charles P. A., Udalski A., 2011, MNRAS, 413, 1600
Reig P., Fabregat J., 2015, A&A, 574, A33
Roy A., Cappallo R., Laycock S. G. T., Christodoulou D. M., Vasilopoulos G., Bhattacharya S., 2022, ApJ, 936, 90
Stahl O., Kaufer A., Tubbesing S., 1999, in Guenther E., Stecklum B., Klose S., eds, Astronomical Society of the Pacific Conference Series Vol. 188, Optical and Infrared Spectroscopy of Circumstellar Matter. p. 331
Straizys V., Kuriliene G., 1981, Ap&SS, 80, 353
Townsend L. J., Coe M. J., Corbet R. H. D., Hill A. B., 2011, MNRAS, 416, 1556
Tsygankov S. S., Lutovinov A. A., Doroshenko V., Mushtukov A. A., Suleimanov V., Poutanen J., 2016, A&A, 593, A16
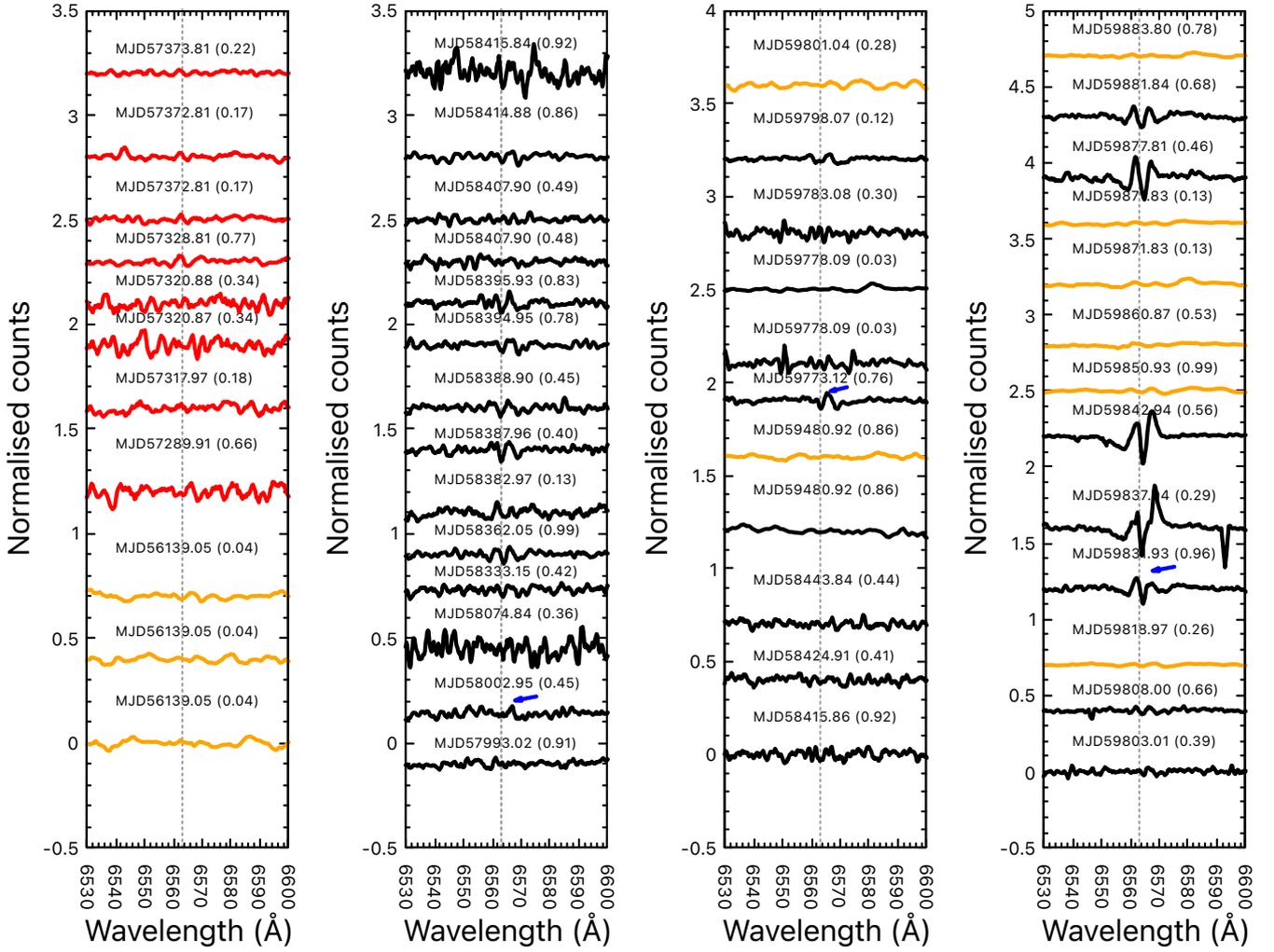
Figure 6. Voigt-subtracted Hα residual spectra. The dashed vertical line in each panel represents the rest lab wavelength of the Hα line. The modified Julian dates and orbital phases were calculated using the ephemeris from Townsend et al. (2011). The blue arrows indicate the epochs of the onset of the redshifted peaks as discussed in Section 3.3. The different colours indicate the different gratings used for the observations: PG0900 (orange), PG1800 (red), and PG2300 (black).

Udalski A., Szymański M. K., Szymański G., 2015, Acta Astron., 65, 1

van den Eijnden J., et al., 2021, MNRAS, 507, 3899

van den Eijnden J., Degenaar N., Russell T. D., Miller-Jones J. C. A., Rouco Escorial A., Wijnands R., Sivakoff G. R., Hernández Santisteban J. V., 2022, MNRAS, 516, 4844

APPENDIX A: TABLES OF X-RAY AND OPTICAL OBSERVATIONS

This paper has been typeset from a TₑX/LATₑX file prepared by the author.

Obs Date MJD	Flux cts/s	Flux error
59744.57	0.87	0.35
59745.37	0.63	0.05
59747.09	0.82	0.04
59757.93	1.91	0.10
59759.92	2.00	0.11
59761.84	2.55	0.15
59763.16	4.11	0.59
59763.27	2.64	0.10
59765.61	3.13	0.19
59765.68	2.13	0.72
59767.21	3.53	0.07
59769.85	3.52	0.07
59771.65	3.24	0.07
59772.77	2.91	0.70
59773.67	3.21	0.38
59773.67	3.00	0.12
59774.13	3.27	0.26
59777.55	2.74	0.14
59778.00	2.21	0.47
59779.57	2.66	0.13
59779.80	1.28	0.49
59781.72	2.31	0.09
59783.67	1.87	0.20
59785.73	1.86	0.05
59786.82	1.45	0.37
59787.69	1.61	0.13
59789.74	1.56	0.05
59791.65	1.09	0.15
59793.24	1.41	0.12
59807.99	0.83	0.04
59809.59	0.96	0.09
59811.90	0.78	0.04
59813.79	0.67	0.04
59814.55	1.05	0.37
59815.74	0.74	0.07
59817.67	0.54	0.04
59819.79	0.53	0.06
59825.03	0.41	0.03
59827.58	0.26	0.02
59830.49	0.12	0.01
59832.78	0.06	0.01

Table A1. Summary of all Swift XRT detections of SMC X-2 during the 2022 outburst

Date	MJD	EW (Å)	Binary phase	RSS grating
2012-07-31	56139.05	-9.96 ± 0.25	0.04	PG0900
2012-07-31	56139.06	-10.54 ± 1.0	0.04	PG0900
2012-07-31	56139.06	-9.83 ± 0.69	0.04	PG0900
2015-09-24	57289.91	-10.40 ± 0.47	0.66	PG1800
2015-10-22	57317.97	-10.33 ± 0.28	0.18	PG1800
2015-10-25	57320.87	-12.51 ± 0.55	0.34	PG1800
2015-10-25	57320.88	-10.97 ± 0.52	0.34	PG1800
2015-11-02	57328.81	-9.57 ± 0.59	0.77	PG1800
2015-12-16	57372.81	-10.67 ± 0.37	0.17	PG1800
2015-12-16	57372.81	-10.58 ± 0.44	0.17	PG1800
2015-12-17	57373.81	-10.88 ± 0.32	0.22	PG1800
2017-08-28	57993.02	-10.29 ± 0.45	0.91	PG2300
2017-09-06	58002.95	-10.05 ± 0.36	0.45	PG2300
2017-11-17	58074.84	-10.12 ± 0.73	0.36	PG2300
2018-08-03	58333.15	-9.74 ± 0.28	0.42	PG2300
2018-09-01	58362.05	-10.19 ± 0.32	0.99	PG2300
2018-09-21	58382.97	-9.89 ± 0.56	0.13	PG2300
2018-09-26	58387.96	-9.65 ± 0.21	0.40	PG2300
2018-09-27	58388.90	-9.07 ± 0.38	0.45	PG2300
2018-10-03	58394.95	-9.55 ± 0.29	0.78	PG2300
2018-10-04	58395.93	-9.11 ± 0.53	0.83	PG2300
2018-10-16	58407.90	-8.81 ± 0.17	0.48	PG2300
2018-10-16	58407.95	-8.77 ± 0.56	0.49	PG2300
2018-10-23	58414.88	-9.79 ± 0.19	0.86	PG2300
2018-10-24	58415.84	-6.88 ± 0.45	0.92	PG2300
2018-10-24	58415.86	-8.88 ± 0.18	0.92	PG2300
2018-11-02	58424.91	-8.29 ± 0.32	0.41	PG2300
2018-11-21	58443.84	-9.44 ± 0.49	0.44	PG2300
2021-09-23	59480.92	-13.15 ± 1.16	0.86	PG0900
2021-09-23	59480.92	-10.95 ± 0.84	0.86	PG0900
2022-07-13	59773.12	-9.46 ± 0.66	0.76	PG2300
2022-07-18	59778.09	-10.26 ± 0.45	0.03	PG2300
2022-07-18	59778.12	-11.72 ± 0.20	0.03	PG2300
2022-07-22	59783.08	-10.29 ± 0.45	0.30	PG2300
2022-08-07	59798.07	-10.00 ± 0.36	0.12	PG2300
2022-08-10	59801.04	-11.75 ± 0.43	0.28	PG0900
2022-08-12	59803.01	-10.35 ± 0.59	0.39	PG2300
2022-08-17	59808.00	-9.98 ± 0.42	0.66	PG2300
2022-08-27	59818.97	-11.47 ± 0.32	0.26	PG0900
2022-09-09	59831.93	-10.79 ± 0.43	0.96	PG2300
2022-09-15	59837.94	-8.52 ± 0.38	0.29	PG2300
2022-09-20	59842.94	-8.40 ± 0.37	0.56	PG2300
2022-09-28	59850.93	-11.15 ± 0.19	0.99	PG0900
2022-10-08	59860.87	-11.16 ± 0.41	0.53	PG0900
2022-10-19	59871.83	-10.80 ± 0.45	0.13	PG0900
2022-10-19	59871.87	-10.04 ± 0.33	0.13	PG0900
2022-10-25	59877.81	-4.05 ± 0.02	0.46	PG2300
2022-10-29	59881.84	-9.32 ± 0.32	0.68	PG2300
2022-10-31	59883.80	-11.14 ± 0.30	0.78	PG0900
2022-11-17	59900.87	-7.09 ± 0.38	0.71	HRS

Table A2. A log of the SALT observations. The Hα equivalent width measurements are recorded and the binary phase determined from the ephemeris in Townsend et al. (2011).

.